

Two ${}^9\text{Li}$ clusters connected with two valence neutrons in ${}^{20}\text{C}$

Naoyuki Itagaki,¹ Tokuro Fukui,¹ Junki Tanaka,² and Yuma Kikuchi³

¹*Yukawa Institute for Theoretical Physics, Kyoto University,
Kitashirakawa Oiwake-Cho, Kyoto 606-8502, Japan*

²*RIKEN Nishina Center for Accelerator-Based Science, 2-1 Hirosawa, Wako, Saitama 351-0198, Japan*

³*Tokuyama College of Technology, Gakuendai, Shunan, Yamaguchi 745-8585, Japan*

(Dated: February 10, 2021)

Many preceding works have shown in ${}^{11}\text{Li}$ the presence of the halo structure comprised of the weakly bound two neutrons around ${}^9\text{Li}$, and it is intriguing to see how this halo structure changes when another ${}^9\text{Li}$ approaches. In this study, we introduce a four-body model for ${}^{20}\text{C}$ with two ${}^9\text{Li}$ clusters and two valence neutrons. The recent development of the antisymmetrized quasi cluster model (AQCM) makes it possible to generate jj -coupling shell-model wave functions from α cluster models. Here, jj -coupling shell model wave function of ${}^9\text{Li}$ is regarded as a cluster, which corresponds to the subclosure configuration of $p_{3/2}$ for the neutrons, and we discuss how the two neutrons connect two ${}^9\text{Li}$ clusters. Until now, most of the clusters in the conventional models have been limited to the closures of the three-dimensional harmonic oscillators, such as ${}^4\text{He}$, ${}^{16}\text{O}$, and ${}^{40}\text{Ca}$; however, owing to AQCM, it is feasible to utilize the jj -coupling shell model wave functions as plural subsystems quite easily. The appearance of a rotational band structure with a cluster structure around the four-body threshold energy is discussed.

I. INTRODUCTION

The ${}^4\text{He}$ nuclei have been known to have large binding energy (28.3 MeV) distinctly in the light mass region. In contrast, it is known that the relative interaction between ${}^4\text{He}$ nuclei is weak. Therefore, they can serve as subsystems in some of the light nuclei, called α cluster structure [1, 2]. The α cluster structure has been studied for decades, and one of the most famous examples is the second 0^+ state of ${}^{12}\text{C}$ with a developed three- α cluster structure [3, 4], which is called the Hoyle state. Many cluster models have proven to be capable of describing various properties of the Hoyle state [5, 6].

In most of the conventional cluster models, however, only the states corresponding to the closure of the three-dimensional harmonic oscillator, such as ${}^4\text{He}$, ${}^{16}\text{O}$, and ${}^{40}\text{Ca}$, have been treated as subsystems called clusters. In these cases, unfortunately, the contribution of the non-central interactions (spin-orbit and tensor interactions), which are quite important in the nuclear systems, vanishes after the antisymmetrization of the wave functions. This is the consequence of the fact that the closure configurations of the major shells are spin-zero systems, and the non-central interactions do not contribute to such spinless systems. In actual nuclear systems, on the contrary, the contribution of the spin-orbit interaction is essential, which enables to explain the observed magic numbers; the subclosure configurations of the jj -coupling shell model ($f_{7/2}$, $g_{9/2}$, and $h_{11/2}$) correspond to the observed magic numbers of 28, 50, and 126 [7]. If we enlarge the model space of the cluster models and open the path to another symmetry, indeed this spin-orbit interaction works as a driving force to break the α clusters, for instance in ${}^{12}\text{C}$ [8].

Therefore, the important task is to include the spin-orbit contribution by extending the traditional cluster models; we proposed the antisymmetrized quasi cluster

model (AQCM) [9–21]. This method allows the smooth transformation of the α cluster model wave functions to jj -coupling shell model ones. We call the clusters that feel the spin-orbit contribution after this transformation quasi clusters. The conventional α cluster models cover the model space of closure of major shells (corresponding to the magic numbers of 2, 8, and 20), and now the subclosure configurations of the jj -coupling shell model, $p_{3/2}$, $d_{5/2}$, $f_{7/2}$, $g_{9/2}$ *etc.*, are covered by our AQCM [15].

The achievement of AQCM allows us to use jj -coupling shell model wave functions as subsystems of the nuclei, which is the beginning of a new cluster model. At first, we have shown the possibility of ${}^{14}\text{C}$, ${}^6\text{He}$, and ${}^9\text{Li}$ as clusters [20, 21], where subclosure configuration of $p_{3/2}$ plays an important role. The cluster structures of ${}^{16}\text{Be}$ (${}^8\text{He}+{}^8\text{He}$), ${}^{17}\text{B}$ (${}^8\text{He}+{}^9\text{Li}$), ${}^{18}\text{C}$ (${}^9\text{Li}+{}^9\text{Li}$), ${}^{24}\text{C}$ (three ${}^8\text{He}$), and ${}^{42}\text{Ar}$ (three ${}^{14}\text{C}$), have been investigated around the corresponding threshold energies.

In this study, we further add neutrons and discuss in ${}^{20}\text{C}$ the ${}^9\text{Li}+{}^9\text{Li}$ cluster configuration as an example. It has been known in ${}^{11}\text{Li}$ that the two neutrons have neutron halo structure around ${}^9\text{Li}$ [22]. It is intriguing to see how such structure is affected when another ${}^9\text{Li}$ approaches to the halo neutrons. In the Be isotopes, it has been extensively discussed that neutrons perform molecular-orbital motion around α clusters; very developed α - α cluster structure appears when two neutrons occupy the σ orbit [23, 24]. This idea can be extended to the linear-chain structure of three α clusters in the C isotopes [25, 26]. If the neutrons in the halo state perform molecular orbital motion around two ${}^9\text{Li}$ clusters with large distances, it paves the way to a novel binding mechanism in the excited states of the neutron-rich nuclei.

This paper is organized as follows. The framework is described in Sec. II. The results are shown in Sec. III. The conclusions are presented in Sec. IV.

II. FRAMEWORK

A. Basic feature of AQCM

AQCM allows the smooth transformation of the cluster model wave functions to the jj -coupling shell model ones. In AQCM, each single particle is described by a Gaussian form as in many other cluster models including the Brink model [1],

$$\phi^{\tau,\sigma}(\mathbf{r}) = \left(\frac{2\nu}{\pi}\right)^{\frac{3}{4}} \exp\left[-\nu(\mathbf{r}-\boldsymbol{\zeta})^2\right] \chi^{\tau,\sigma}, \quad (1)$$

where the Gaussian center parameter $\boldsymbol{\zeta}$ is related to the expectation value of the position of the nucleon, and $\chi^{\tau,\sigma}$ is the spin-isospin part of the wave function. For the size parameter ν , here we use $\nu = 0.20 \text{ fm}^{-2}$, which gives the optimal 0^+ energy of ^{12}C within a single AQCM basis state. The Slater determinant is constructed from these single-particle wave functions by antisymmetrizing them.

Next, we focus on the Gaussian center parameters $\{\boldsymbol{\zeta}_i\}$. As in other cluster models, here four single-particle wave functions with different spin and isospin sharing a common $\boldsymbol{\zeta}$ value correspond to an α cluster. This cluster wave function is transformed into jj -coupling shell model based on the AQCM. When the original value of the Gaussian center parameter $\boldsymbol{\zeta}$ is \mathbf{R} , which is real and related to the spatial position of this nucleon, it is transformed by adding the imaginary part as

$$\boldsymbol{\zeta} = \mathbf{R} + i\Lambda \mathbf{e}^{\text{spin}} \times \mathbf{R}, \quad (2)$$

where \mathbf{e}^{spin} is a unit vector for the intrinsic-spin orientation of this nucleon. The control parameter Λ is associated with the breaking of the cluster, and with a finite value of Λ , the two nucleons with opposite spin orientations have the $\boldsymbol{\zeta}$ values, which are complex conjugate with each other. This situation corresponds to the time-reversal motion of two nucleons. After this transformation, the α clusters are called quasi clusters. We can generally create the single-particle orbits of the jj -coupling shell model by taking the limits of $\mathbf{R} \rightarrow 0$ and $\Lambda \rightarrow 1$.

B. Wave function for ^{20}C

The total wave function for ^{20}C is the superposition of different Slater determinants, $\{\Phi_i\}$,

$$\Psi_{J\pi} = \sum_{i,K} c_i^K P_{J\pi}^K \Phi_i. \quad (3)$$

All Slater determinants are projected to the eigen states of parity and angular momentum by using the projection operator $P_{J\pi}^K$,

$$P_{J\pi}^K = P^\pi \frac{2J+1}{8\pi^2} \int d\Omega D_{MK}^J R(\Omega). \quad (4)$$

Here D_{MK}^J is the Wigner D -function and $R(\Omega)$ is the rotation operator for the spatial and spin parts of the wave function. This integration over the Euler angle Ω is numerically performed. The operator P^π is for the parity projection ($P^\pi = (1 + P^r)/\sqrt{2}$ for the positive-parity states, where P^r is the parity-inversion operator), which is also performed numerically. The coefficients $\{c_i^K\}$ are obtained together with the energy eigenvalue E when we diagonalize the norm and Hamiltonian (H) matrices, namely by solving the Hill-Wheeler equation.

$$\sum_{i,j,K,K'} (\langle \Phi_i | (P_{J\pi}^{K'})^\dagger H P_{J\pi}^K | \Phi_j \rangle - E \langle \Phi_i | (P_{J\pi}^{K'})^\dagger P_{J\pi}^K | \Phi_j \rangle) c_j^K = 0. \quad (5)$$

This angular momentum projection enables to generate different K number states as independent basis states from each Slater determinant.

Each Slater determinant consists of the antisymmetrized product of single-particle wave functions.

$$\Phi_i = \mathcal{A} \{ \phi^{\tau_1,\sigma_1}(\mathbf{r}_1, \boldsymbol{\zeta}_1) \phi^{\tau_2,\sigma_2}(\mathbf{r}_2, \boldsymbol{\zeta}_2) \cdots \phi^{\tau_{19},\sigma_{19}}(\mathbf{r}_{19}, \boldsymbol{\zeta}_{19}) \phi^{\tau_{20},\sigma_{20}}(\mathbf{r}_{20}, \boldsymbol{\zeta}_{20}) \}_i. \quad (6)$$

Here, the single-particle wave functions from $\phi^{\tau_1,\sigma_1}(\mathbf{r}_1, \boldsymbol{\zeta}_1)$ to $\phi^{\tau_9,\sigma_9}(\mathbf{r}_9, \boldsymbol{\zeta}_9)$ belong to one ^9Li cluster, whereas those from $\phi^{\tau_{10},\sigma_{10}}(\mathbf{r}_{10}, \boldsymbol{\zeta}_{10})$ to $\phi^{\tau_{18},\sigma_{18}}(\mathbf{r}_{18}, \boldsymbol{\zeta}_{18})$ are for another ^9Li . For each ^9Li cluster, we introduce the subclosure configuration of $(s_{1/2})^2(p_{3/2})^4$ for the neutrons. For the proton part, the last protons in two ^9Li clusters are introduced as time-reversal configurations, $|3/2 \ 3/2\rangle$ and $|3/2 \ -3/2\rangle$. Then these two ^9Li clusters are separated with the relative distance of d_i , which is randomly generated with equal probability between 0.5 fm and 5.0 fm.

The two valence neutrons, $\phi^{\tau_{19},\sigma_{19}}(\mathbf{r}_{19}, \boldsymbol{\zeta}_{19})$ and $\phi^{\tau_{20},\sigma_{20}}(\mathbf{r}_{20}, \boldsymbol{\zeta}_{20})$, are introduced to have opposite spin directions (spin-up and spin-down). Their Gaussian center parameters ($\boldsymbol{\zeta}_{19}$ and $\boldsymbol{\zeta}_{20}$) are generated by using random numbers $\{r_k\}$, which have the probability distribution $P(|r_k|)$ proportional to $\exp[-|r_k|/\sigma]$,

$$P(|r_k|) \propto \exp[-|r_k|/\eta]. \quad (7)$$

The value of η is chosen to be 1.5 fm which corresponds to the standard deviation of 3.67 fm. After generating $\{r_k\}$, we multiply the sign factor to each r_k , which allows r_k to be positive and negative with equal probability. The resultant random numbers are applied to all three (x , y , z) components of the Gaussian center parameters of the two valence neutrons.

C. Hamiltonian

The Hamiltonian consists of the kinetic energy and potential energy terms. For the potential part, the interaction consists of the central (\hat{V}_{central}), spin-orbit ($\hat{V}_{\text{spin-orbit}}$), and Coulomb terms. For the central part,

the Tohsaki interaction [27] is adopted. This interaction has finite ranges for the three-body terms in addition to two-body terms, which is designed to reproduce both saturation properties and scattering phase shifts of two α clusters. For the spin-orbit part, we use the spin-orbit term of the G3RS interaction [28], which is a realistic interaction originally developed to reproduce the nucleon-nucleon scattering phase shifts.

The Tohsaki interaction consists of two-body ($V^{(2)}$) and three-body ($V^{(3)}$) terms:

$$\hat{V}_{\text{central}} = \frac{1}{2} \sum_{i \neq j} V_{ij}^{(2)} + \frac{1}{6} \sum_{i \neq j, j \neq k, i \neq k} V_{ijk}^{(3)}, \quad (8)$$

where $V_{ij}^{(2)}$ and $V_{ijk}^{(3)}$ have three ranges,

$$V_{ij}^{(2)} = \sum_{\alpha=1}^3 V_{\alpha}^{(2)} \exp \left[-\frac{(\vec{r}_i - \vec{r}_j)^2}{\mu_{\alpha}^2} \right] \left(W_{\alpha}^{(2)} - M_{\alpha}^{(2)} P^{\sigma} P^{\tau} \right)_{ij}, \quad (9)$$

$$V_{ijk}^{(3)} = \sum_{\alpha=1}^3 V_{\alpha}^{(3)} \exp \left[-\frac{(\vec{r}_i - \vec{r}_j)^2}{\mu_{\alpha}^2} - \frac{(\vec{r}_i - \vec{r}_k)^2}{\mu_{\alpha}^2} \right] \times \left(W_{\alpha}^{(3)} - M_{\alpha}^{(3)} P^{\sigma} P^{\tau} \right)_{ij} \left(W_{\alpha}^{(3)} - M_{\alpha}^{(3)} P^{\sigma} P^{\tau} \right)_{ik}. \quad (10)$$

Here, $P^{\sigma} P^{\tau}$ represents the exchange of the spin-isospin part of the wave functions of interacting two nucleons. The physical coordinate for the i th nucleon is \vec{r}_i . The details of the parameters are shown in Ref. [27], but we use F1' parameter set for the Majorana parameter ($M_{\alpha}^{(3)}$) of the three-body part introduced in Ref. [9].

The G3RS interaction [28] is a realistic interaction, and the spin-orbit term has the following form;

$$\hat{V}_{\text{spin-orbit}} = \frac{1}{2} \sum_{i \neq j} V_{ij}^{ls}, \quad (11)$$

where

$$V_{ij}^{ls} = \left(V_{ls}^1 e^{-d_1(\vec{r}_i - \vec{r}_j)^2} - V_{ls}^2 e^{-d_2(\vec{r}_i - \vec{r}_j)^2} \right) P(^3O) \vec{L} \cdot \vec{S}. \quad (12)$$

Here, \vec{L} is the angular momentum for the relative motion between the i th and j th nucleons, and \vec{S} is the sum of the spin operator for these two interacting nucleons. The operator $P(^3O)$ stands for the projection onto the triplet-odd state. The strength of the spin-orbit interactions is set to $V_{ls}^1 = V_{ls}^2 = 1800$ MeV, which allows consistent description of ^{12}C and ^{16}O [9].

III. RESULTS

A. Energy convergence of ^{20}C

We start the discussion with the 0^+ energy curves of ^{20}C calculated with the present $^9\text{Li}+^9\text{Li}+n+n$ model.

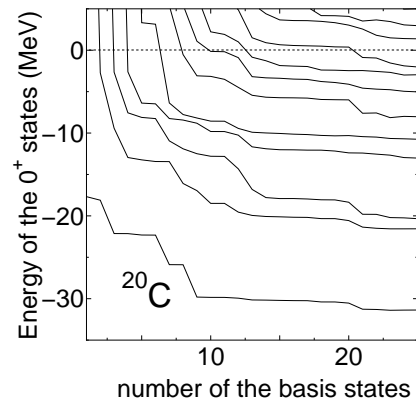


FIG. 1. Energy curves for the 0^+ states of ^{20}C calculated with the $^9\text{Li}+^9\text{Li}+n+n$ model. Horizontal axis shows the number of Slater determinants superposed. Energies are measured from the four-body threshold.

The horizontal axis of Fig. 1 shows the number of Slater determinants superposed, and for each Slater determinant, the distances between two ^9Li (d) and the positions for the Gaussian center parameters for the two valence neutrons (ζ_{19} and ζ_{20}) are randomly generated. The energies are measured from the four-body threshold. This calculation is based on the bound state approximation and it could be possible that some of the obtained states above the neutron threshold are continuum states, but the states with flat energies after rapid convergence are candidates for the resonance states. The lowest 0^+ state converges to -31.4 MeV, and experimentally, the ground state of ^{20}C is located at -28.5 MeV from the threshold. The obtained 0^+ energies are summarized in Table I.

B. Principal quantum number of the harmonic oscillator

We discuss the property of each state obtained after superposing the basis states. Particular focus is placed on the point which states have the character of $^9\text{Li}+^9\text{Li}$ cluster configuration. One of the physical quantities, which characterize each state, is the expectation value of the principal quantum number \hat{N} of the harmonic oscillator,

$$\hat{N} = \sum_i \mathbf{a}_i^\dagger \cdot \mathbf{a}_i. \quad (13)$$

The summation can be taken independently for the proton part and neutron part. In Table I, the column “ N -proton” stands for the expectation value of \hat{N} for the protons and “ N -neutron” for the neutrons. The lowest Pauli-allowed values are 4 for the protons (two are in the s -shell and four are in the p -shell) and 18 for the neutrons (two are in the s -shell, six are in the p -shell, and six are in the sd -shell). The lowest 0^+ state has the values of 4.19 (protons) and 18.61 (neutrons) fairly close to the lowest Pauli-allowed values, which indicates that the state has

TABLE I. Properties of 0^+ states of ^{20}C obtained by superposing Slater determinants. The energies are measured from the $^9\text{Li} + ^9\text{Li} + n + n$ threshold (E (MeV)). Expectation values of the principal quantum number for the proton part (N -proton) and neutron part (N -neutron) are listed together with those of the single-particle parity of the protons (spp -proton) and neutrons (spp -neutron).

	E (MeV)	N -proton	N -neutron	spp -proton	spp -neutron
1	-31.37	4.19	18.61	-1.90	1.85
2	-21.56	4.43	18.92	-1.78	1.87
3	-20.34	4.90	19.82	-1.56	1.64
4	-13.02	4.83	19.86	-1.58	1.06
5	-10.75	5.60	21.41	-1.27	-0.79
6	-8.03	4.71	19.62	-1.59	1.49
7	-5.03	5.68	21.44	-1.29	1.04
8	-2.96	6.12	21.79	-0.35	0.08
9	-2.02	5.77	21.68	-1.13	1.15
10	1.38	5.96	22.13	-1.09	0.89

pure shell-model character. However, the excited states have much larger values.

It should be stressed that the principal quantum number N for the protons (N -proton) is governed by the distance between two ^9Li clusters, since protons are only in the ^9Li clusters and the internal wave functions of each ^9Li is frozen except for the antisymmetrization effect. Thus, the N -proton values listed in Table I is considered to contain information for the distance between two ^9Li clusters, although the expectation values are obtained after superposing Slater determinants with different ^9Li - ^9Li distances. To extract the contribution of the $^9\text{Li} + ^9\text{Li}$ core part, in Fig. 2, we show the N values of ^{18}C without the two valence neutrons as a function of the distance between two ^9Li clusters (Fig. 2(a): protons and Fig. 2(b): neutrons). At the zero-limit for the distance d between two ^9Li , the values are 4 (protons) and 14 (neutrons), The values increase to 4.9 (protons) and 15.7 (neutrons) at $d = 3$ fm, and they grow to 5.6 and 16.9 at $d = 3.5$ fm (they further increase to 6.6 and 18 at $d = 4$ fm).

According to Table I, the fifth state at -10.75 MeV, seventh state at -5.03 MeV, eighth state at -2.96 MeV, ninth state at -2.02 MeV, and tenth state at 1.38 MeV have the N -proton values of $5.5 - 6.0$. Thus, it is quite likely that these states have the cluster structure with the ^9Li - ^9Li distances of $3.5 - 4.0$ fm. Among them, the eighth state at -2.96 MeV has the largest N -proton value of 6.12, and we consider this state as a candidate for the cluster state representing these states. The N -proton value of 6.12 corresponds to the ^9Li - ^9Li distances of 3.75 fm in ^{18}C without the valence neutrons (Fig. 2(a)). In our preceding work for ^{18}C [21], $^9\text{Li} + ^9\text{Li}$ cluster state has been shown to appear slightly below the corresponding threshold energy. Therefore, it is rather reasonable to

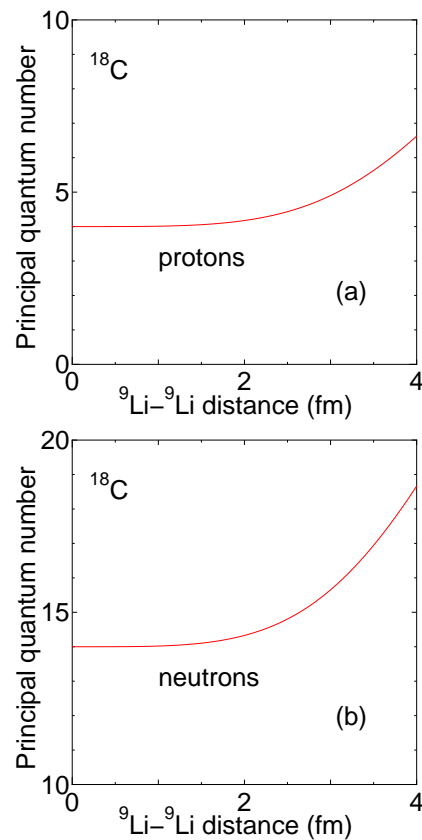


FIG. 2. Principal quantum number N of the harmonic oscillator for the 0^+ state of ^{18}C as a function of the distance between two ^9Li clusters. (a): protons and (b): neutrons.

find here the appearance of the cluster state in ^{20}C after adding two valence neutrons to ^{18}C below the four-body threshold. This state shows rapid energy convergence in Fig 1, which is considered to be a possible resonance state.

If we assume that the 0^+ state of ^{20}C at -2.96 MeV, which is the candidates for the cluster state, has the ^9Li - ^9Li distances of about 3.75 fm, the neutrons in the $^9\text{Li} + ^9\text{Li}$ core part must have the N -neutron value around 17.75 (Fig. 2(b)). Therefore, we can deduce the contribution of the two valence neutrons in the state at -2.96 MeV by subtracting 17.75 from the N -neutron value of 21.79 listed in Table I. The two valence neutrons are estimated to have the N value of about 4.0 in the cluster state, and each valence neutron shares the value of ~ 2.0 . Thus, it turns out that valence neutrons remain in two-node orbits as in the ground state.

C. Single-particle parity

To discuss the properties of the two valence neutrons in ^{20}C in more detail, next we calculate the single-particle parity. In this framework, the single-particle orbits introduced are non-orthogonal, and therefore we cannot

directly discuss the parity of each orbit. Another difficulty of directly discussing the parity of each single-particle comes from the superposition of Slater determinants performed here. Nevertheless, we can get insights for the single-particle parity from the expectation value of the single-particle operator, which is the sum of the parity inversion operator for each nucleon [29],

$$\hat{O}^{spp} = \sum_i P_i^r. \quad (14)$$

Here P_i^r is the parity-inversion operator for the i -th nucleon. The eigenvalues of P_i^r is 1 and -1 , for the positive-parity orbit and negative-parity orbit, respectively. The summation can be taken over the protons or neutrons independently.

We calculate the expectation value of this single-particle parity for the 0^+ states of ^{20}C listed in Table I, which are obtained by superposing Slates determinants. In Table I, the column “*spp*-proton” is for the protons and “*spp*-neutron” is for the neutrons. The ground state has the values of -1.90 (protons) and 1.85 (neutrons) indicating that the state has the character of the lowest shell-model state. In the lowest shell-model state, two protons and two neutrons are in the s -shell with positive-parity, four protons and six neutrons are in the p -shell with negative-parity, and six neutrons are in the sd -shell with positive-parity, and hence, the single-particle parity becomes $2 - 4 = -2$ for the protons and $2 - 6 + 6 = 2$ for the neutrons. However, the candidates for the cluster state (eighth states at -2.96 MeV in Table I identified as cluster state in the previous subsection) has quite different values; -1.09 (*spp*-proton) and 0.08 (*spp*-neutron).

In the present model, the protons are only in the $^9\text{Li} + ^9\text{Li}$ core part as mentioned before. Thus, the calculated single-particle parity of the protons (*spp*-proton) is governed by the distance between two ^9Li clusters. The correspondence between the distance between two ^9Li clusters and *spp*-proton can be clarified in ^{18}C by removing the two valence neutrons. Figure 3 depicts the single-particle parity for the 0^+ state of ^{18}C as a function of the distance between two ^9Li clusters, where the dotted line is for the protons (*spp*-proton) and the dashed-line is for the neutrons (*spp*-neutron). For the protons (dotted line), the value is around -2 at small relative distances because the last proton in each ^9Li occupies p -shell-like one-node orbit. However the value starts slightly deviating from -2 with increasing the distance, suggesting partial excitation of the protons to two-node orbits with positive-parity, while the total parity of the two- ^9Li system is always projected to positive. The value for the protons is -1.60 at the $d = 3.5$ fm and it becomes -0.97 at $d = 4$ fm.

We can compare this result with the *spp*-proton values of ^{20}C listed in Table I, where the two valence neutrons are added and the states with different ^9Li - ^9Li distances are superposed. In the previous subsection, we have identified that the eighth state in Table I as the candidates for the cluster state with the ^9Li - ^9Li distances of ~ 3.75 fm.

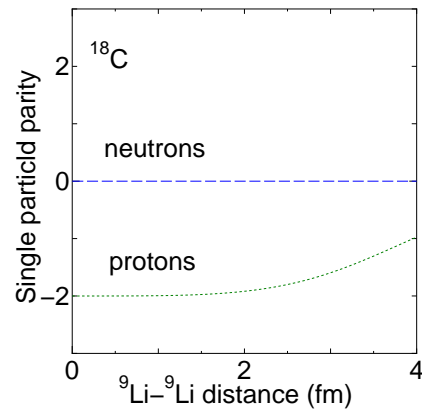


FIG. 3. Single-particle parity for the 0^+ state of ^{18}C as a function of the distance between two ^9Li clusters. Dotted line is for the protons and dashed-line is for the neutrons.

The obtained *spp*-proton values of ^{20}C is -0.35 for the eighth state, quite different from -2 . The obtained value is consistent with that for the states having finite ^9Li - ^9Li distances, suggesting the prominent cluster structure.

Next, we discuss the single-particle parity of the neutron part. It is intriguing to point out that in ^{18}C without the two valence neutrons, the single-particle parity of the neutrons is always zero independent of the ^9Li - ^9Li distance (Fig. 3 dashed line). This is coming from the fact that the neutrons in both ^9Li have identical (sub-closure) configurations except for the central positions of the clusters. The antisymmetrization effect allows the linear combination of the single-particle orbits, and the combinations of the two orbits with good parity around the center of left or right cluster always create a pair of positive-parity and negative-parity orbits. Thus, the single-particle parity for the neutrons of ^{18}C is zero, and in ^{20}C , the *spp*-neutron values purely show the contribution of the two valence neutrons. In Table I, the ground state and low excited states have the value close to 2 indicating that the two valence neutrons are in the sd -shell-like positive-parity orbits. However, the candidate for the cluster state (eighth state in Table I) have the value of 0.08 completely different from 2. The result indicates that the valence neutrons have more complex characters than “pure two-node orbits”, which was not evident when we discussed the principal quantum number N in the previous subsection. One of the possible explanations is that the orbits of the valence neutrons have mixed components of the p -shell, sd -shell, and pf -shell orbits.

D. Rotational band structure of ^{20}C

The same calculation can be performed also for the 2^+ and 4^+ states of ^{20}C . The eighth states in Table I at -2.96 MeV, which is a candidate for the cluster structure, serves as a band head state of a rotational band

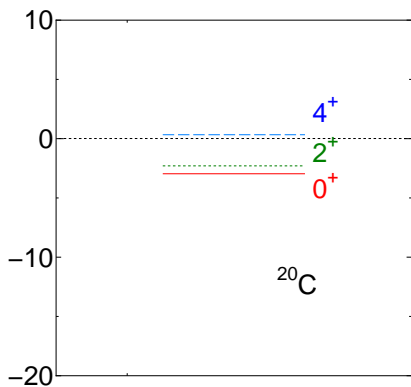


FIG. 4. Rotational band structure of ^{20}C measured from the $^9\text{Li} + ^9\text{Li} + n + n$ threshold energy. Solid, dotted, and dashed lines are for 0^+ , 2^+ , and 4^+ states.

structure as shown in Fig. 4, where the solid, dotted, and dashed lines are for 0^+ , 2^+ , and 4^+ states, respectively. The 2^+ state at -2.29 MeV and 4^+ states at 0.33 MeV are connected with the 0^+ state at -2.96 MeV and classified into a rotational band judging from the similarity of the calculated properties (principal quantum number and single-particle parity) and electromagnetic transition probabilities among the states. We have not considered the energy of each state in this classification, but eventually, typical level spacings of the rotational band structure comes out around the $^9\text{Li} + ^9\text{Li} + n + n$ threshold energy. The rotational band shows small level spacings between 0^+ and 2^+ reflecting the large deformation.

IV. CONCLUSIONS

In this study, we discussed the structure of ^{20}C by introducing a four-body cluster model with $^9\text{Li} + ^9\text{Li} + n + n$ configurations. The recent development of the antisym-

metrized quasi cluster model (AQCM) enables us to utilize jj -coupling shell-model wave functions as plural subsystems quite easily. Until now, many works have shown in ^{11}Li the presence of the halo structure comprised of the weakly bound two neutrons around ^9Li , and our study was motivated by a question how this halo structure changes when another ^9Li approaches.

In our preceding work for ^{18}C [21], it has been discussed that $^9\text{Li} + ^9\text{Li}$ cluster state appears below the threshold, and therefore, it is natural in ^{20}C to see the appearance of the cluster states below the threshold after adding the two valence neutrons. The candidate for the cluster state was identified by calculating the principal quantum number and single-particle parity. The candidate for the cluster state serves as a band head state and forms a rotational band structure, where the members are collected by the similarity of the properties and electromagnetic transition probabilities among the states. The states have small level spacings reflecting the large deformation.

As future work, we investigate the possibility of molecular-orbital states. In the present analysis, we discussed that atomic-orbit states, where neutron(s) sticks to one of the two centers, but in the molecular-orbit state, each valence neutron rotates around two centers equally with good parity. Such molecular-orbit states are expected to appear around the threshold energy. Also, we will connect the calculation to the nuclear reaction and discuss how we can populate these states in the actual experiment.

ACKNOWLEDGMENTS

The authors would like to thank the discussion with Dr. M. Sasano (RIKEN). The numerical calculations have been performed using the computer facility of Yukawa Institute for Theoretical Physics, Kyoto University.

-
- [1] D. M. Brink, Proc. Int. School Phys. “Enrico Fermi” **XXXVI**, 247 (1966).
 - [2] M. Freer, H. Horiuchi, Y. Kanada-En’yo, D. Lee, and U.-G. Meißner, Rev. Mod. Phys. **90**, 035004 (2018).
 - [3] F. Hoyle, Astrophys. J. Suppl. **1**, 121 (1954).
 - [4] M. Freer and H. Fynbo, Prog. Part. Nucl. Phys. **78**, 1 (2014).
 - [5] Y. Fujiwara, H. Horiuchi, K. Ikeda, M. Kamimura, K. Katō, Y. Suzuki, and E. Uegaki, Prog. Theor. Phys. Supplement **68**, 29 (1980).
 - [6] A. Tohsaki, H. Horiuchi, P. Schuck, and G. Röpke, Phys. Rev. Lett. **87**, 192501 (2001).
 - [7] M. G. Mayer and H. G. Jensen, “Elementary theory of nuclear shell structure”, John Wiley, Sons, New York, Chapman, Hall, London (1955).
 - [8] N. Itagaki, S. Aoyama, S. Okabe, and K. Ikeda, Phys. Rev. C **70**, 054307 (2004).
 - [9] N. Itagaki, Phys. Rev. C **94**, 064324 (2016).
 - [10] N. Itagaki, H. Masui, M. Ito, S. Aoyama, and K. Ikeda, Phys. Rev. C **73**, 034310 (2006).
 - [11] H. Masui and N. Itagaki, Phys. Rev. C **75**, 054309 (2007).
 - [12] T. Yoshida, N. Itagaki, and T. Otsuka, Phys. Rev. C **79**, 034308 (2009).
 - [13] N. Itagaki, J. Cseh, and M. Płoszajczak, Phys. Rev. C **83**, 014302 (2011).
 - [14] T. Suhara, N. Itagaki, J. Cseh, and M. Płoszajczak, Phys. Rev. C **87**, 054334 (2013).
 - [15] N. Itagaki, H. Matsuno, and T. Suhara, Prog. Theor. Exp. Phys. **2016**, 093D01 (2016).
 - [16] H. Matsuno, N. Itagaki, T. Ichikawa, Y. Yoshida, and Y. Kanada-En’yo, Prog. Theor. Exp. Phys. **2017**, 063D01 (2017).
 - [17] H. Matsuno and N. Itagaki, Prog. Theor. Exp. Phys.

- 2017**, 123D05 (2017).
- [18] N. Itagaki and A. Tohsaki, Phys. Rev. C **97**, 014307 (2018).
- [19] N. Itagaki, H. Matsuno, and A. Tohsaki, Phys. Rev. C **98**, 044306 (2018).
- [20] N. Itagaki, A. V. Afanasjev, and D. Ray, Phys. Rev. C **101**, 034304 (2020).
- [21] N. Itagaki, T. Fukui, J. Tanaka, and Y. Kikuchi, Phys. Rev. C **102**, 024332 (2020).
- [22] I. Tanihata, H. Hamagaki, O. Hashimoto, Y. Shida, N. Yoshikawa, K. Sugimoto, O. Yamakawa, T. Kobayashi, and N. Takahashi, Phys. Rev. Lett. **55**, 2676 (1985).
- [23] N. Itagaki and S. Okabe, Phys. Rev. C **61**, 044306 (2000).
- [24] M. Ito, N. Itagaki, H. Sakurai, and K. Ikeda, Phys. Rev. Lett. **100**, 182502 (2008).
- [25] N. Itagaki, S. Okabe, K. Ikeda, and I. Tanihata, Phys. Rev. C **64**, 014301 (2001).
- [26] P. W. Zhao, N. Itagaki, and J. Meng, Phys. Rev. Lett. **115**, 022501 (2015).
- [27] A. Tohsaki, Phys. Rev. C **49**, 1814 (1994).
- [28] R. Tamagaki, Prog. Theor. Phys. **39**, 91 (1968).
- [29] N. Itagaki, W. von Oertzen, and S. Okabe, Phys. Rev. C **74**, 067304 (2006).